

See discussions, stats, and author profiles for this publication at: <https://www.researchgate.net/publication/271510796>

# Solid-State NMR Study of Hydroxyapatite Containing Amorphous Phosphate Phase and Nanostructured Hydroxyapatite: Cut-Off Averaging of CP-MAS Kinetics and Size Profiles of Spin Clust...

ARTICLE *in* THE JOURNAL OF PHYSICAL CHEMISTRY C · NOVEMBER 2014

Impact Factor: 4.77 · DOI: 10.1021/jp510229f

---

CITATION

1

---

READS

68

## 1 AUTHOR:



Vytautas Klimavičius

Vilnius University

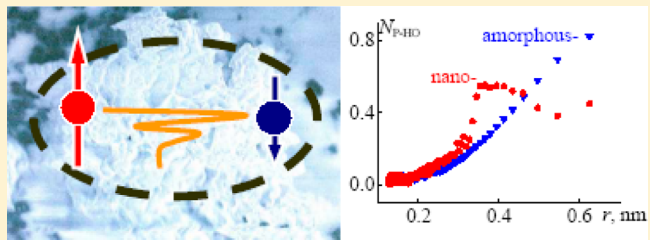
9 PUBLICATIONS 20 CITATIONS

[SEE PROFILE](#)

# Solid-State NMR Study of Hydroxyapatite Containing Amorphous Phosphate Phase and Nanostructured Hydroxyapatite: Cut-Off Averaging of CP-MAS Kinetics and Size Profiles of Spin Clusters

Vytautas Klimavicius,<sup>†</sup> Aivaras Kareiva,<sup>‡</sup> and Vytautas Balevicius<sup>\*,†</sup><sup>†</sup>Department of General Physics and Spectroscopy, Vilnius University, Sauletekio 9-3, LT-10222 Vilnius, Lithuania<sup>‡</sup>Department of Inorganic Chemistry, Vilnius University, Naugarduko 24, LT-03225 Vilnius, Lithuania

**ABSTRACT:** High data point density measurements of  $^1\text{H}$ - $^{31}\text{P}$  cross-polarization kinetics have been carried out for calcium hydroxyapatite containing amorphous phosphate phase (ACP-CaHA) and nanostructured hydroxyapatite (CaHA). The chosen setting of the sampling frequency of  $5 \times 10^4 \text{ s}^{-1}$  allowed us to reveal all spin interactions having the dipolar splitting  $b \leq 25 \text{ kHz}$ , which in the case of  $^1\text{H}$ - $^{31}\text{P}$  interaction means the structures with the internuclear distances  $r \geq 0.125 \text{ nm}$  could be resolved. The advanced processing of CP-MAS kinetic data has been developed, introducing the variable cutoff distribution of the dipolar coupling. This procedure allows us to describe the oscillatory kinetics and CP curves in nanostructured materials over a wide range of contact time and to determine the characteristic size profile and composition of the spin clusters. The characteristic size of  $^{31}\text{P}-(^1\text{H})_n$  spin nanocluster being within 0.3 to 0.5 nm has been determined for nanostructured CaHA. The nonclassical spin coupling model is more preferable to describe the CP kinetics in ACP-CaHA.



## INTRODUCTION

Materials based on calcium phosphates have found many applications in implantology, orthopedic, and periodontal surgery.<sup>1–4</sup> A special place in these areas occupies calcium hydroxyapatite ( $\text{Ca}_{10}(\text{PO}_4)_6(\text{OH})_2$ , further CaHA), which shows close similarity to the mineral of hard tissues (bone, enamel, dentin, etc.) and therefore has high biocompatibility with them.<sup>5</sup> Stoichiometric CaHA is a reference compound for the apatite mineral group.<sup>2</sup>

NMR techniques have been widely exploited studying various structural aspects and dynamics of these compounds over the last two to three decades. The great potential of  $^{43}\text{Ca}$  NMR in the structure analysis of calcium hydroxyapatites and related systems has been revealed.<sup>6,7</sup> However, the majority of NMR studies, such as the signal shift and shape analysis, heteronuclear correlations (HETCOR), cross-polarization (CP), and so on, have been carried out on  $^1\text{H}$  and  $^{31}\text{P}$  nuclei. (See refs 2–4 and 8–11 and refs cited therein). CP kinetics studies provide maybe the most valuable information on relaxation, spin-diffusion, and fine details of structural organization in these systems.

Cross-polarization (CP) is a solid-state NMR technique originally developed for enhancing the peak intensities of rare nuclei by the polarization transfer from abundant nuclei, typically from protons.<sup>12,13</sup> CP is also feasible between abundant nuclei. In such case, the CP enhancement is ineffective and sometimes the signals can be even weaker than those obtained from a conventional single pulse-acquire Bloch-decay (BD) experiments.<sup>2,8</sup> However, the CP technique between abundant nuclei is very useful in physical character-

ization of solid materials having complex structures. Very important comments to practical considerations of CP kinetics and modeling are given in the review article of Kolodziejski and Klinkowski (ref 8). The review of the existing literature allows us to resume: there are significant number of works containing incorrectly performed variable contact time experiments (insufficient number of sampling points, especially for very short contact times) and improper kinetic curve fittings using various CP models; the nonclassical model,<sup>8</sup> which would be more appropriate in many cases, is not popular. Dense contact time sampling often reveals faint-to-moderate intensity oscillations from the incompletely averaged dipolar couplings, and this problem becomes more intriguing applying MAS technique.

For these reasons, two calcium hydroxyapatites (containing amorphous phosphate phase<sup>14–16</sup> (ACP-CaHA) and nanostructured CaHA) have been synthesized and studied in the present work using solid-state  $^1\text{H}$  and  $^{31}\text{P}$  NMR spectroscopy having the purposes: (i) to measure high data point density of  $^1\text{H}$  and  $^{31}\text{P}$  NMR spectra and  $^1\text{H}$ - $^{31}\text{P}$  cross-polarization kinetics, (ii) to develop proper methods of processing of CP MAS data that would allow us to describe the oscillatory kinetics and CP curves in nanostructured materials over the wide range of contact time; and (iii) to determine the

Received: October 10, 2014

Revised: November 17, 2014

Published: November 18, 2014



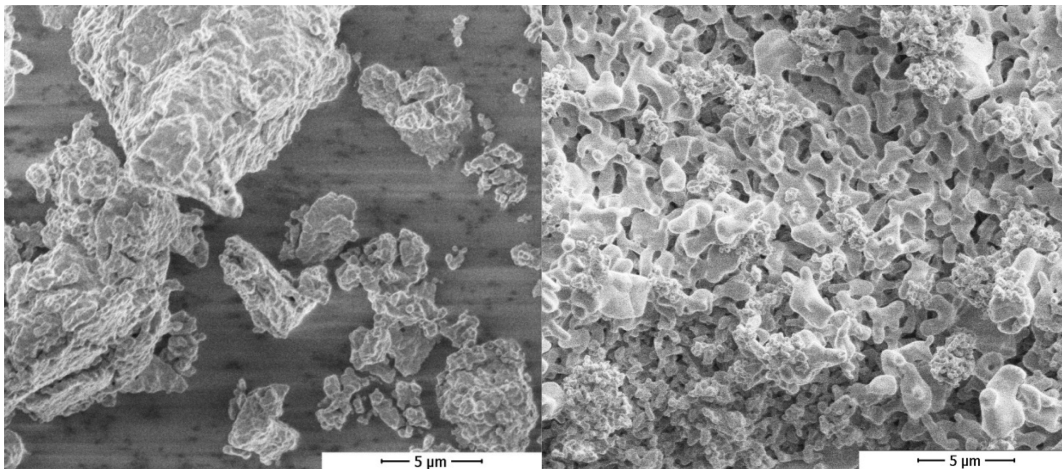


**Figure 1.** SEM micrographs of CaHA samples prepared by Synthesis I (on the left) and Synthesis II (on the right).

characteristic size profile and composition of the spin clusters in nanostructured materials.

## ■ EXPERIMENTAL SECTION

NMR measurements were carried out on Bruker AVANCE III HD spectrometer operating at resonance frequencies of 400 and 162 MHz for  $^1\text{H}$  and  $^{31}\text{P}$ , respectively, at 298 K. The  $^1\text{H}$  90° pulse length was 2.5  $\mu\text{s}$ , and 64 scans were accumulated with repetition delay of 3 s. The repetition delay in  $^1\text{H}$ – $^{31}\text{P}$  CP experiments was 2 s, and 16 scans were accumulated. The pulse length in  $^{31}\text{P}$  BD with decoupling experiments was 1.8  $\mu\text{s}$ , and 16 scans with repetition delay of 10 s were accumulated. MAS measurements were performed at 5 kHz for  $^1\text{H}$ – $^{31}\text{P}$  CP and 10 kHz for  $^1\text{H}$  BD. A rectangular variable contact time pulse shape was used in CP-MAS experiments. Supplementary static NMR experiments were performed. The Hartmann–Hahn condition was matched at second-order sidebands. NMR spectra were processed using Topsin 3.2 software. The signal shapes and CP kinetic curves were processed using Microcal Origin 9 and Mathcad 15 packages.

**Materials.** For the preparation of  $\text{Ca}_{10}(\text{PO}_4)_6(\text{OH})_2$  having different morphological features, two sol–gel synthesis routes were selected. Calcium hydroxyapatite containing amorphous phosphate phase has been prepared by Synthesis I: In the sol–gel process, calcium acetate monohydrate,  $\text{Ca}(\text{CH}_3\text{COO})_2 \cdot \text{H}_2\text{O}$ , and ammonium hydrogen phosphate,  $(\text{NH}_4)_2\text{HPO}_4$ , were selected as Ca and P sources, respectively, in Ca/P mole ratio 1.67. First, calcium acetate monohydrate was dissolved in distilled water under continuous stirring at 65 °C. After stirring at 60–65 °C for 1 h, the glycerol,  $\text{C}_3\text{H}_8\text{O}_3$ , as complexing agent dissolved in 50 mL of distilled water was added. Finally, the appropriate amount of  $(\text{NH}_4)_2\text{HPO}_4$  was added to the above solution. The obtained solution was stirred in a beaker covered with watch glass for 10 h at the same temperature. After evaporation of solvent, the transparent white gels were obtained. The gels were dried in an oven for 10 h at 110 °C. The obtained powders were ground in agate mortar and heated to 800 °C for 5 h and repeatedly two times at 1000 °C for 5 h. Nanostructured CaHA has been obtained from Synthesis II: In the sol–gel process, the same starting materials as those in the Synthesis I were selected. The mixture of calcium acetate and ammonium hydrogen phosphate was stirred at 60–65 °C for 1 h. Instead of glycerol, the tartaric acid was selected as complexing agent. Obtained mixture was vigorously stirred

for 12 h at 60–65 °C in a beaker covered with a watch glass. After evaporation of solvent, the transparent white gels were obtained. The gels were dried in an oven for 10 h at 110 °C. The obtained powders were grinded in agate mortar and heated to 800 °C for 5 h and repeatedly two times at 1000 °C for 5 h. The synthesis products were characterized by scanning electron microscopy (SEM) and energy-dispersive X-ray analysis (EDX) using a Helios NanoLab 650 scanning electron microscope coupled to energy-dispersive X-ray spectrometry system. SEM micrographs of CaHA samples prepared by Synthesis I and II are shown in Figure 1.

The EDX spectra obtained for the ACP-CaHA and nanostructured CaHA samples showed that only calcium, phosphorus, and oxygen are present in both of the samples, and no other elements can be detected from the EDX spectra. These results initially suggested that the synthesized samples are of high purity and good quality. However, the Ca/P molar ratios of the synthesized samples based on EDX analysis are as follows 1.59 (Synthesis I) and 1.67 (Synthesis II). For stoichiometric amorphous calcium phosphate and CaHA, the Ca/P ratios are 1.5 and 1.67, respectively. As seen, for the obtained nanostructured CaHA powders, the Ca/P ratio is 1.67 and fits very well with the calculated one. Moreover, many separate parts or particles of ACP-CaHA sample showed Ca/P ratios about 1.5. Therefore, the EDX analysis data confirmed that the ACP-CaHA samples are composed of two phosphates, where the main crystalline phase is CaHA.

X-ray diffraction (XRD) data were collected in the range of  $20 \leq 2\theta \leq 80^\circ$  using Ni-filtered  $\text{CuK}_\alpha$  radiation on Rigaku MiniFlex II diffractometer working in Bragg–Brentano ( $\theta/2\theta$ ) geometry. The XRD patterns of the samples after calcination of Ca–P–O gels obtained at 1000 °C are shown in Figure 2. As it is seen, both XRD diffraction patterns mostly contain diffraction lines attributable to calcium hydroxyapatite. The obtained results are in a good agreement with the reference data for  $\text{Ca}_{10}(\text{PO}_4)_6(\text{OH})_2$  (PDF [72–1243]). However, only Synthesis II gave single-phase CaHA product. The EDX analysis results showed that the calcination products at 1000 °C of Ca–P–O gels obtained from Syntheses II besides desirable  $\text{Ca}_{10}(\text{PO}_4)_6(\text{OH})_2$  phase contained some amount of side calcium and phosphorus containing particles. However, these phases are not detectable in the XRD pattern and therefore could be attributed to the amorphous or amorphous-clustered calcium phosphate phases.<sup>17,18</sup>

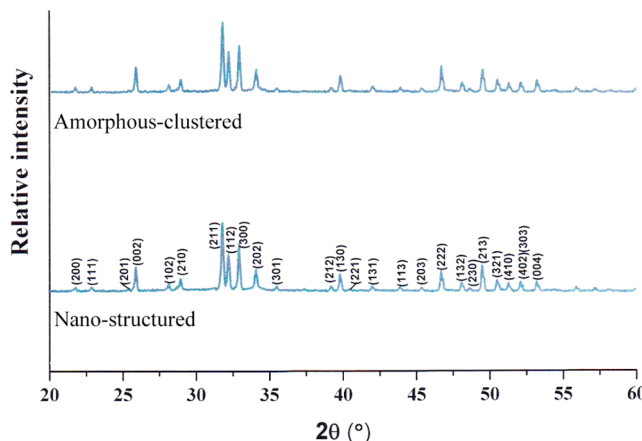


**Figure 2.** XRD patterns of ACP-CaHA and nanostructured CaHA samples.

The average grain size ( $d$ ) of these powders is also calculated by the well-known Scherrer's formula

$$d = \frac{0.9\lambda}{\beta \cos(\theta)} \quad (1)$$

where  $\lambda$  is the wavelength of Cu K $\alpha$ ,  $\beta$  is the full width at half-maximum of the peak intensity, and  $\theta$  is the Bragg's diffraction angle. From the XRD pattern of the synthesized phosphate powders calcined at 1000 °C, the average of crystallite size was calculated to be  $\sim 103 \pm 5$  nm for nanostructured CaHA and  $\sim 183 \pm 9$  nm for ACP-CaHA. The crystallinity index of synthesized samples was calculated according to ref 19. Nanostructured CaHA powders with crystallinity degree  $X_c \approx 83\%$  were prepared using sol–gel method, while the degree of crystallinity of ACP-CaHA powders was calculated to be  $X_c \approx 69\%$ . However, this method of determination of crystallinity degree is very sensitive to the crystallite dimensions.<sup>19</sup> For absolute quantification by powder X-ray diffraction of amorphous–crystalline mixtures, all relevant sample-radiation interaction phenomena could be considered as well.<sup>20</sup> The accuracy of determination of crystallinity degree of amorphous–crystalline mixtures is also very much dependent on the volume fraction of amorphous or crystalline phases.<sup>21</sup>

Both samples, prepared in these ways, can be compared with respect to the structural organization of hydroxyl groups. This is important analyzing  $^1\text{H} \rightarrow ^{31}\text{P}$  CP MAS kinetics. As it is clearly seen in  $^1\text{H}$  MAS spectra (Figure 3), the amount of structural hydroxyl groups (a sharp peak at 0.0 ppm) in nanostructured CaHA is significantly higher than that from adsorbed water (a broad signal at  $\sim 5$  ppm).

The amount of structural hydroxyl groups in ACP-CaHA is practically negligible in comparison with adsorbed water. It cannot be excluded that in the presence of a large amount of adsorbed water in the sample the  $^1\text{H}$  signal of structural –OH can be significantly broadened due to dynamic exchange processes and thus hardly seen in the spectrum. Several minor peaks seen in the spectra of both samples at 0.5–3.0 ppm were also observed for other hydroxyapatites.<sup>2,10</sup> However, as it was noted there, their assignment is still controversial. Most probably, they are originated from highly mobile or too distant to  $^{31}\text{P}$  protons.<sup>2</sup>

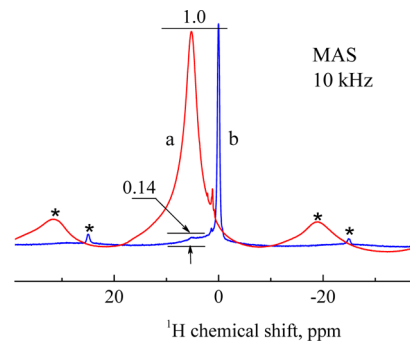


**Figure 3.**  $^1\text{H}$  MAS NMR spectra of ACP-CaHA (red) and nanostructured CaHA (blue).

## RESULTS AND DISCUSSION

The variable  $^1\text{H} \rightarrow ^{31}\text{P}$  contact time experiments were performed using the sampling frequency of  $5 \times 10^4$  s $^{-1}$ . According to the Nyquist's theorem, this setting allows us to reveal all spin interactions having the dipolar splitting  $b \leq 25$  kHz. It means that in the case of  $^1\text{H} \rightarrow ^{31}\text{P}$  interaction the structures with the spin distances  $r \geq 0.125$  nm could be resolved. Each experimental CP kinetic curve contains at this setting 500 points over the whole contact time range 10  $\mu\text{s}$  to 10 ms (Figure 4). Such high data point density reduces excess degrees of freedom in the nonlinear signal contours fitting procedure

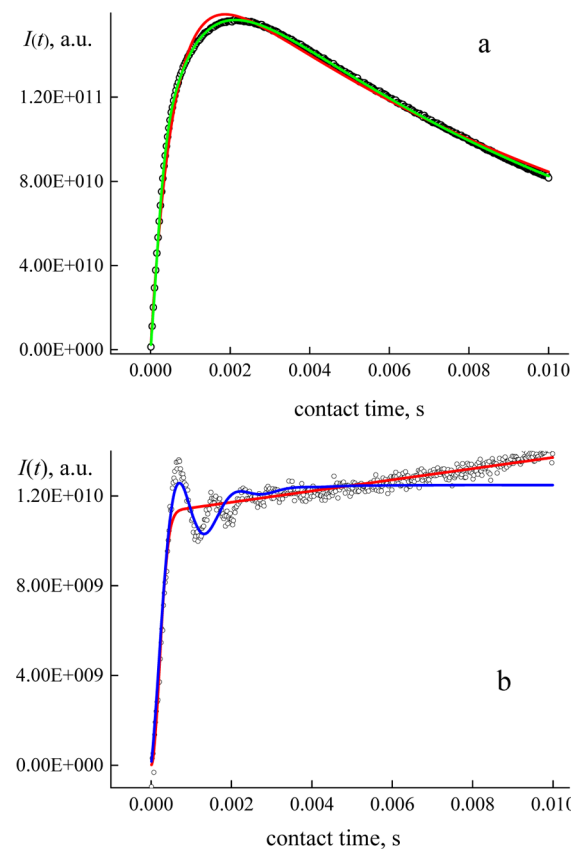


**Figure 4.**  $^1\text{H} \rightarrow ^{31}\text{P}$  CP MAS kinetics (integrated central  $^{31}\text{P}$  signal intensities versus variable contact time) in ACP-CaHA (a) and in nanostructured CaHA (b). The fitting for ACP-CaHA was carried out using eq 7 (green line) and the classical I–S model<sup>8</sup> (red line). The fitting for nanostructured CaHA was carried out using eqs 3 (blue line) and 7 (red line). The fit parameters are presented in Table 1

targeting its flow toward the “true” (global) minimum on the multiparameter surface  $\chi^2$ , that is, the sum of weighted squares of deviations of the chosen theoretical model curve from the experimental points. It makes possible more rigorous decision concerning the validity of the hypothetic models (signal shapes), and more fitting parameters can be used and determined unambiguously.

Before starting to analyze CP kinetics, some comments concerning the integrated signal intensities and the optimal MAS rate should be done. The  $^{31}\text{P}$  MAS NMR spectra of nanoapatites often contain composite lines. For several systems, it succeeded in decomposing the observed  $^{31}\text{P}$  signal into two to three spectral components.<sup>4,9–11</sup> A precise signal shape analysis has been carried out in the present work for both studied samples using a huge experimental data set; viz. each experimental  $^{31}\text{P}$  spectrum contained  $\sim 100$  points/ppm ( $>4000$  points per contour). Three signal components are also visible in  $^{31}\text{P}$  MAS spectrum of nanostructured CaHA in BD experiment; however, applying CP the signal at  $\sim 4$  ppm is drastically weakened up to ca. 5% of the central peak intensity and the peak at  $\sim 1$  ppm disappears (Figure 5). Therefore, the

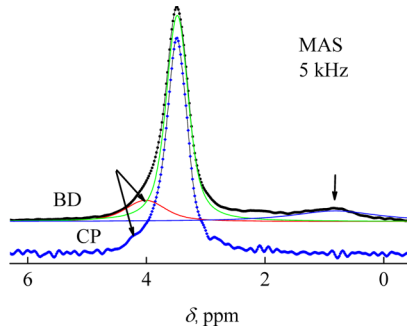


**Figure 5.**  $^{31}\text{P}$  MAS spectra of nanostructured CaHA in BD and CP experiments. The arrows mark the presence of signal components beside the central peak.

integral intensities of only the central dominant peaks were used, constructing the kinetic curves (Figure 4). The central dominant  $^{31}\text{P}$  NMR peak was found to be a single Voigt shape having a perfect fit to experiment ( $R^2 \cong 0.990$  to 0.999). Moreover, it was found that the relative contributions of Lorentz and Gauss components in the Voigt profile depends on the spinning rate. This signal shape evolution stops at  $\sim 3$  kHz spinning for ACP-CaHA and at  $\sim 5$  kHz for nanostructured CaHA. Therefore, it was decided to accept the MAS rate of 5 kHz as the optimal one for both samples.

The CP kinetics in ACP-CaHA (Figure 4a) looks very similar to that observed in polycrystalline brushite and some other systems.<sup>8</sup> This curve consists of three characteristic parts: fast rise, slow rise, and decay. The CP kinetics observed in the nanostructured CaHA exhibit the damped oscillation of intensity in the short contact time range (Figure 4b).

The oscillations of CP intensity have been observed for the first time in  $^1\text{H} \rightarrow ^{13}\text{C}$  CP experiments on single crystals.<sup>22,23</sup> It was deduced that the frequency of oscillation depends on the orientation of the crystal in the external magnetic field, and it is equal to one-half of the dipolar splitting ( $b$ ). Later on, such oscillations have been found for many other systems, including powders, bilayers, and other complex structured solids. (See refs 8 and 10.) The oscillatory CP kinetics for an isolated pair of spins 1/2 can be described by the equation<sup>22</sup>

$$I(t) = I_0 e^{-t/T_{1\rho}} \left[ 1 - \frac{1}{2} e^{-t/T_{\text{dif}}} - \frac{1}{2} e^{-3t/2T_{\text{dif}}} \cos\left(\frac{2\pi b t}{2}\right) \right] \quad (2)$$

where  $T_{1\rho}$  is the spin-lattice relaxation time in the rotating frame,  $T_{\text{dif}}$  is the spin-diffusion time constant, and  $b$  is the dipolar coupling (in hertz). The original eq 2 has been modified for S-I<sub>n</sub> spin clusters<sup>8</sup> by introducing the parameter  $\lambda$  that describes the cluster composition

$$I(t) = I_0 e^{-t/T_{1\rho}} [1 - \lambda e^{-t/T_{\text{dif}}} - (1 - \lambda) e^{-3t/2T_{\text{dif}}} \cos(2\pi b t/2)] \quad (3)$$

This parameter depends also on molecular dynamics and therefore  $\lambda$  values must be optimized during the kinetic curve fitting procedure.<sup>2,8,10</sup>

To apply eq 3 to process the CP kinetic data for complex solids it has to be averaged over the whole distribution of  $b$  that depends on the spatial parameters (internuclear distance ( $r$ ) and orientation in the magnetic field ( $\theta$ ))

$$b = \frac{\mu_0 \gamma_I \gamma_S \hbar}{4\pi r^3} \frac{(1 - 3\cos^2 \theta)}{2} = D_{IS} \frac{(1 - 3\cos^2 \theta)}{2} \quad (4)$$

The averaged value of  $\cos(2\pi b t/2)$  is obtained, summing its values weighted by the fraction of spin pairs with a set of spatial parameters that corresponds to the oscillation frequency  $b_i$

$$\overline{\cos\left(\frac{2\pi b t}{2}\right)} = \frac{\sum_i I(b_i/2) \cos(2\pi b_i t/2)}{\sum_i I(b_i/2)} \quad (5)$$

An elegant trick for this averaging is given in ref 24, which leads to the Gauss decay with the time constant  $T_2$

$$\overline{\cos\left(\frac{2\pi b t}{2}\right)} \cong \exp\left(-\frac{t^2}{T_2^2}\right) \quad (6)$$

that should be valid for very short contact times. Hence the  $b$ -averaged eq3 can be written as

$$I(t) = I_0 e^{-t/T_{1\rho}} [1 - \lambda e^{-t/T_{\text{dif}}} - (1 - \lambda) e^{-3t/2T_{\text{dif}}} e^{-t^2/2T_2^2}] \quad (7)$$

The above eqs 3 and 7 describe the kinetics of CP in the frame of so-called nonclassical I–I<sup>\*</sup>–S model,<sup>8</sup> where the asterisk denotes protons in close neighborhood to S spins ( $^{31}\text{P}$  in the present case). The I<sup>\*</sup>–S spin pairs or clusters exchange polarization in an oscillatory manner. The oscillations are damped by the subsequent spin diffusion. This model has been proposed in addition to the more popular classical I–S model, where it is assumed that spin-diffusion is fast enough to force spins to behave as a system at a uniform spin temperature.<sup>8,25</sup> Comparing both models it is seen that the I–I<sup>\*</sup>–S model is appropriate when the heteronuclear I<sup>\*</sup>–S spin interactions are strong compared with homonuclear I–I ones. In the case of weak I–S and moderate or strong I–I couplings, the CP kinetics is better described using the classical I–S model. More details concerning both models, their validity, and applications are given in ref 8.

Equation 7 was successfully applied processing the CP kinetic curves of various complex systems. A nice fit to experimental points sampled over a wide range contact time (up to  $\sim 20$  ms) was achieved in many cases.<sup>2,8</sup> Also, in the present work, eq 7 perfectly ( $R^2 = 0.9997$ ) fits to the experimental points of CP kinetics in ACP-CaHA over the whole contact time range up to 10 ms (Figure 4a). This

**Table 1.** Fit Data for CP MAS Kinetics of Hydroxyapatite Containing Amorphous Phosphate Phase and Nanostructured Hydroxyapatite (Figure 4)

Hydroxyapatites Containing Amorphous Phosphate Phase (ACP-CaHA)					
model: nonclassical I-I*-S, eq 7, present work; $R^2 = 0.9997$			model: classical I-S, see eqs 4–7 in ref 8; $R^2 = 0.993$		
parameter	value	standard error	parameter	value	standard error
$I_0$ , au	$2.09217 \times 10^{11}$	$2.67333 \times 10^8$	$I_0$ , au	$2.2675 \times 10^{11}$	
$\lambda$	0.69785	0.00303	$T_{is}$ , s	$7.84059 \times 10^{-4}$	$1.21223 \times 10^{-5}$
$T_{dip}$ , s	0.00102	$6.83182 \times 10^{-6}$	$T_{1\rho}^I$ , s	0.0089	$1.49841 \times 10^{-4}$
$T_{1\rho}$ , s	0.01075	$2.16237 \times 10^{-5}$	$T_{1\rho}^S$ , s	$\infty$	
$T_2$ , s	$2.37958 \times 10^{-4}$	$1.97806 \times 10^{-6}$	$\epsilon\alpha^2$	0.22986	0.00605
			$I_{00}$ , au <sup>a</sup>	$6.23775 \times 10^9$	$1.08322 \times 10^9$

Nanostructured Hydroxyapatites (CaHA)					
model: nonclassical I-I*-S, eq 7, present work; $R^2 = 0.940$			model: nonclassical I-I*-S, eq 3, present work; $R^2 = 0.950$		
parameter	value	standard error	parameter	value	standard error
$I_0$ , au	$2.33336 \times 10^{11}$		$I_0$ , a.u.	$1.24871 \times 10^{10}$	
$\lambda$	0.95191	$2.06532 \times 10^{-4}$	$\lambda$	0.40228	0.00732
$T_{dip}$ , s	0.884	0.02877	$T_{dip}$ , s	0.001	$1.94717 \times 10^{-5}$
$T_2$ , s	$2.09845 \times 10^{-4}$	$3.55254 \times 10^{-6}$	$b$ , Hz	1365.64736	16.7895
$T_{1\rho}$ , s	$\infty$		$T_{1\rho}$ , s	$\infty$	

<sup>a</sup>Intensity zero-line correction. This extra fitting parameter has been added to the above ones used in ref 8.

experimental curve was tried to fit using the classical I-S model of CP dynamics between two abundant nuclei.<sup>8,25</sup> A nice coincidence with experiment ( $R^2 = 0.993$ ) and quite realistic values of the fit parameters have been obtained using this model as well (Table 1). However, some systematic (non-random) deviations are noticeable in the middle part of curve, that is, at slow rise (1–3 ms) and in the decay part at 8–10 ms (Figure 4a), despite the fact that more fitting parameters were included. These systematic discrepancies were possible to be revealed only thanks to the high experimental point density as previously noted. Hence it can be concluded that the I-I\*-S model is more preferable to describe the CP kinetics in ACP-CaHA.

The oscillation of intensity is well-expressed in the CP kinetic curve of the nanostructured CaHA (Figure 4b). Unfortunately, it was not succeeded to describe the observed kinetics by eqs 3 and 7 over the whole contact time range. The initial part of the curve up to  $\sim 5$  ms can be more or less approached by eq 3 reproducing the oscillation. The fit value  $b = 1366 \pm 17$  Hz (see Table 1) is close to those determined for some synthetic hydroxyapatites with doped carbonate and magnesium ions.<sup>10</sup> However, note that the present curve does not reach plateau at the contact time above  $\sim 5$  ms. Such behavior differs from the kinetics observed there. The discrepancy between experimental and calculated (eq 3) values diverges, getting into the range of longer contact times (Figure 4b). The situation is opposite, trying to fit the data using eq 7. The good fit was achieved over the whole range of contact time, but the oscillation was lost. This is because the averaging by summing over a broad spectrum of  $b$  values (eq 5) yields destructive interference that blurs the oscillation pattern. It is obvious that the new treatment of CP data, an intermediate one to eqs 3 and 7, has to be created to describe the CP kinetics in the nanostructured systems over a wide dynamic range.

This can be done by noticing that the summing of the weighted cosine values (eq 5) can be considered as discrete cosine Fourier transform of function  $I(b/2)$  from  $b$ - to  $t$ -domain

$$\begin{aligned} & \frac{\sum_i I\left(\frac{b_i}{2}\right) \cos\left(\frac{2\pi b_i t}{2}\right)}{\sum_i I\left(\frac{b_i}{2}\right)} \\ & \rightarrow \frac{1}{A} \sum_i^\infty I\left(\frac{b_i}{2}\right) \cos\left(2\pi \frac{b_i}{2} t\right) \\ & = \text{ReFT}\left\{ I\left(\frac{b}{2}\right) \right\} \end{aligned} \quad (8)$$

where  $A = \sum_i I(b_i/2)$  is the normalizing factor. The summing can be formally extended to infinity prolonging  $I(b/2)$  by the proper zero-filling.

The  $^{31}\text{P}$  NMR signal being perfectly Gauss- or Voigt-shaped with significant Gauss contribution clarifies why eq 6 so perfectly describes the experimental points sampled over very wide range of contact time although the averaging (eq 6) has been derived in the short time limit.<sup>24</sup> It is well known that the Fourier transform of Gauss function produces the Gauss function. This means that the relation (eq 6) and thus the eq 7 must be valid in the cases of Gauss-shaped  $I(b/2)$  without any limitation in time. To support this, we have checked for the static samples, that is, in the case where the signal shape is mainly determined by the dipole-dipole interactions, the full widths at half-maximum (fwhm) obtained by fitting of  $^{31}\text{P}$  signal shape by Voigt function and  $T_2$  that follows from the processing of CP kinetic curve using eq 7 (4020 Hz and  $8.8 \times 10^{-5}$  s (ACP-CaHA); 2560 Hz and  $1.4 \times 10^{-4}$  s (nanostructured CaHA)) obey  $\text{fwhm} \cdot T_2 = 0.375$  (the case of exact Gauss functions). Namely,  $\text{fwhm} \cdot T_2 \approx 0.355$  was found to be almost the same for both samples.

Because of spatial structural discontinuities in nanomaterials, the dipole coupling distribution  $I(b/2)$  can be rather complex. Its shape can be determined replacing the Gauss decay (eq 6) in eq 7 by Fourier image (eq 8) and performing an inverse Fourier transform from  $t$  to  $b$  domain

$$I(b/2) \sim \left| \widehat{\text{FT}}^{-1} \frac{1 - \lambda f_1 - I(t)/I_0 f_3}{(1 - \lambda)f_2} \right| \quad (9)$$

where  $f_1 = \exp(-t/T_{\text{dif}})$ ,  $f_2 = \exp(-1.5t/T_{\text{dif}})$ , and  $f_3 = \exp(-t/T_{1\rho})$ . To apply eq 9, the values of  $I_0$ ,  $\lambda$ ,  $T_{\text{dif}}$  and  $T_{1\rho}$  have to be known. At the first approach, the necessary values can be taken from the set of fit parameters obtained using eq 7 (Table 1); knowing that this equation describes the CP kinetics over the whole range of contact time, only the oscillation is blurred (Figure 4b). Later those values can be refined.

The results of the experimental data processing using eq 9 are presented in Figure 6. A distinct difference between  $I(b)$  for

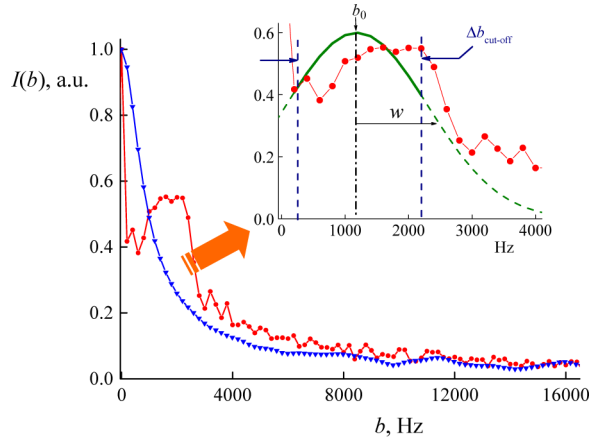


**Figure 6.** Dipole–dipole coupling distributions in ACP-CaHA (blue) and in nanostructured CaHA (red). More comments in the text.

both samples is the broad band centered at  $\sim 1500$  Hz for the nanostructured CaHA, whereas the monotonic decay is observed for ACP-CaHA. The most convenient choice is to approximate that the top part of the broad band is the Gauss function  $G(b_i) = \exp(-(b_i - b_0)^2/2w^2)$  with the adjustable parameters  $b_0$  and  $w$ . However, its “long tails” have to be cut off at the certain  $b$  values. (See the inset part in Figure 6.) For this purpose, the parameter  $\Delta b_{\text{cutoff}}$  was introduced. It is easy to realize that the  $\Delta b_{\text{cutoff}}$  value is characteristic of each nanostructured system and must be also optimized during the CP kinetic curve fitting using

$$I(t) = I_0 e^{-t/T_{1\rho}} \left[ 1 - \lambda e^{-t/T_{\text{dif}}} - (1 - \lambda e)^{-3t/2T_{\text{dif}}} \right] \frac{\sum_i^{\Delta b_{\text{cutoff}}} G(b_i) \cos(2\pi b_i t / 2)}{\sum_i^{\Delta b_{\text{cutoff}}} G(b_i)} \quad (10)$$

Equation 10 indeed can be considered as an intermediate one to eqs 3 and 7: asymptotically, if  $G(b) \rightarrow \delta(b - b_0)$ , it becomes eq 3 and one gets eq 7 if  $G(b)$  is the “true” Gauss function.

The fitting of CP kinetics in the nanostructured CaHA using eq 10 with the whole set of parameters has been carried out. The result is presented in Figure 7. This fitting refines the values of the parameters that initially were taken from the set obtained using eq 7, which, unfortunately, does not reproduce the oscillation part in the CP kinetics. A nice fit and more realistic values of the used parameters have been obtained. For example, the spin-diffusion time constant  $T_{\text{dif}} = 0.88$  s that follows eq 6 was applied (Table 1) and drops to 7.6 ms. This value gets into the same time scale deduced for the related nanocrystalline HAs.<sup>2,10</sup> Also, note that the infinitely long  $T_{1\rho}$  came out even without the presence of plateau in the kinetics curve. The  $\lambda$  value has also been changed significantly. For rigid

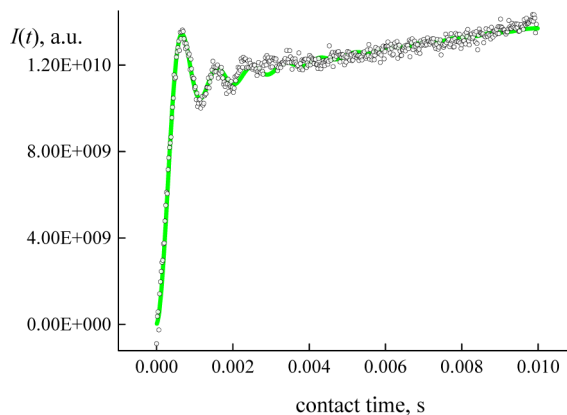


**Figure 7.**  $^1\text{H} \rightarrow ^{31}\text{P}$  CP MAS kinetics in nanostructured CaHA. The fitting was carried out using the complete set of parameters and eq 9. The fit parameter values are  $\Delta b_{\text{cutoff}} = 2050$  Hz,  $b_0 = 1185$  Hz,  $w = 1115$  Hz,  $I_0 = 1.5 \times 10^{10}$ ,  $\lambda = 0.348$ ,  $T_{\text{dif}} = 7.6$  ms, and  $T_{1\rho} \rightarrow \infty$ . The value of  $R^2 = 0.989$  was achieved.

structures, the parameter  $\lambda = 1/(n + 1)$ , where  $n$  is the number of protons in the spin cluster interacting with  $^{31}\text{P}$  nucleus (for systems studied in the present work). Using the refined value of  $\lambda = 0.348$ , the number of protons can be evaluated  $n = 1.87$ , which is lower than what would follow from the general formula  $(\text{Ca}_{10}(\text{PO}_4)_6(\text{OH})_2)$ . This can be caused by the previously discussed different MAS effect on the  $^{31}\text{P}$  interaction with protons in the structural hydroxyls and adsorbed water.

The  $\lambda$  value was determined using the  $b$ -averaged CP kinetics (eq 10). The major contribution in the averaging comes from  $I(b)$  at  $b_0 = 1185$  Hz within  $\Delta b_{\text{cutoff}} = 2050$  Hz (Figure 6). This part of  $I(b)$  is mainly contributed from the incompletely averaged dipolar couplings, that is, from  $^{31}\text{P}$  interactions with more mobile protons.

The MAS technique fails to suppress anisotropic spin interactions fully if intensive reorientational dynamics is present.<sup>26</sup> The interactions of  $^{31}\text{P}$  spins with the protons in structural hydroxyl groups, that is, more tightly bonded to phosphorus, are essentially averaged by MAS. It contributes the increase in the peak in the distribution  $I(b)$  at  $b = 0$ . The molecules of adsorbed water possess much higher degree of motional freedom. In the presence of reorientational motion the MAS line shape and width become dependent on the spin interaction strength, the time scale of the motion, and the spinning rate.<sup>26</sup> This effect was noticed and already previously mentioned discussion about the optimal MAS rate. Hence, despite the fact the  $\lambda$  value was optimized, it is still likely that  $\lambda$  can be considered only as a certain qualitative (not quantitative) parameter that can be useful comparing the cluster composition in series of related systems.

The obtained dipole coupling distribution (Figure 6) can be used deducing some structural aspects of the studied systems. The internuclear distances can be calculated from eq 4 if the corresponding dipolar coupling constants are known. In the case of isolated pairs of spins the magnitude of the coupling constant is directly deduced from the Pake-like pattern obtained by Fourier transform of the oscillatory polarization transfer.<sup>27</sup> For a powder sample, under MAS the dipolar coupling (eq 4) becomes

$$b_{\pm 2} = \frac{D_{\text{IS}}}{2} \sin^2 \beta \quad (11)$$

where  $\pm 2$  means a second-order sideband matching and  $\beta$  is the angle between  $r$  and the rotor axis. The maximum splitting that corresponds to  $\beta = \pi/2$  is half of the splitting between the intense singularities in a Pake pattern.<sup>27</sup> In the presence of nanostructuring effects the Pake-like pattern is partially blurred due to disorder in the internuclear distances. The complex-shaped contour  $I(b)$  found for nanostructured CaHA (Figure 6) can be considered as the envelope of the superposition of Pake singularities from the pairs of spins having different internuclear distances. The obtained dipole coupling distribution allows us to determine the characteristic size profile of the spin clusters in ACP-CaHA and in nanostructured CaHA. They are presented in Figure 8.

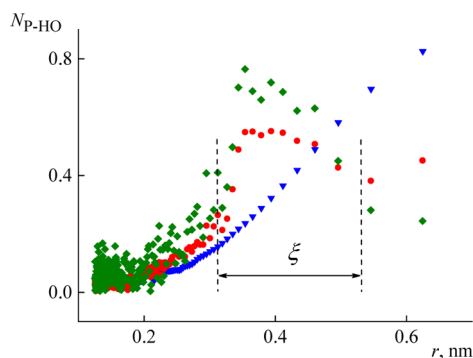


**Figure 8.** Spatial distribution of protons surround  $^{31}\text{P}$  nuclei in ACP-CaHA (blue) and nanostructured CaHA (red, obtained using the first approach parameter values; green, using the refined values). The characteristic size of  $^{31}\text{P}-(^1\text{H})_n$  spin nanocluster is denoted as  $\xi$ .

The characteristic size of  $^{31}\text{P}-(^1\text{H})_n$  spin nanocluster being within  $\xi = 0.3$  to 0.5 nm has been determined for the nanostructured CaHA. It should be noted that the size profile is not crucially influenced by the refinement of parameters  $I_0$ ,  $\lambda$ ,  $T_{\text{diff}}$  and  $T_{1\rho}$  (Figure 8). It is also rather interesting to note that the initial slope of CP dynamics in biomimetic hydroxyapatite–gelatin nanocomposites was well described using the average  $^{31}\text{P}-^1\text{H}$  distance of 0.53 nm (concerning that two protons are  $\sim 0.4$  nm apart and four other are at  $\sim 0.6$  nm).<sup>4</sup>

## CONCLUSIONS

(1) High data point density measurements of  $^1\text{H}-^{31}\text{P}$  cross-polarization kinetics have been carried out for calcium hydroxyapatite containing amorphous phosphate phase (ACP-CaHA) and nanostructured calcium hydroxyapatites (CaHA). The chosen setting of the sampling frequency allowed us to resolve the  $^1\text{H}-^{31}\text{P}$  cluster structures with the internuclear distances  $r \geq 0.125$  nm.

(2) The advanced processing of CP MAS data has been developed introducing the variable cutoff distribution of the dipolar coupling. The characteristic size of  $^{31}\text{P}-(^1\text{H})_n$  spin cluster being within 0.3 to 0.5 nm has been determined for nanostructured CaHA.

(3) The nonclassical spin coupling model is more preferable to describe the CP kinetics in the calcium hydroxyapatites containing amorphous phosphate phase.

(4) The developed treatment can be very useful searching for the best complexing agents, controlling fine structural features and the perfectness of synthesized nanostructures in series of related materials.

## AUTHOR INFORMATION

### Corresponding Author

\*E-mail: vytautas.balevicius@ff.vu.lt.

### Notes

The authors declare no competing financial interest.

## ACKNOWLEDGMENTS

Funding from the European Community's social foundation under grant agreement no. VP1-3.1-ŠMM-08-K-01-004/KS-120000-1756 is acknowledged. We thank Aleksandr Momot for the preparation of the materials.

## REFERENCES

- (1) Le Geros, R. Z. *Calcium Phosphates in Oral Biology and Medicine*; Karger: Basel, 1991.
- (2) Kolmas, J.; Kolodziejski, W. Inverse  $^{31}\text{P} \rightarrow ^1\text{H}$  NMR Cross-Polarization in Hydrated Nanocrystalline Calcium Hydroxyapatite. *Chem. Phys. Lett.* **2012**, *554*, 128–132.
- (3) Mathew, R.; Gunawidjaja, P. N.; Izquierdo-Barba, I.; Jansson, K.; Garcia, A.; Arcos, D.; Vallet-Regi, M.; Eden, M. Solid-State  $^{31}\text{P}$  and  $^1\text{H}$  NMR Investigations of Amorphous and Crystalline Calcium Phosphates Grown Biomimetically From a Mesoporous Bioactive Glass. *J. Phys. Chem. C* **2011**, *115*, 20572–20582.
- (4) Vyalikh, A.; Simon, P.; Kollmann, T.; Kniep, R.; Scheler, U. Local Environment in Biomimetic Hydroxyapatite-Gelatin Nanocomposites As Probed by NMR Spectroscopy. *J. Phys. Chem. C* **2011**, *115*, 1513–1519.
- (5) Brown, P. W.; Constantz, B. *Hydroxyapatite and Related Materials*; CRC Press: Boca Raton, FL, 1994.
- (6) Laurencin, D.; Wong, A.; Dupree, R.; Smith, M. E. Natural Abundance  $^{43}\text{Ca}$  Solid-State NMR Characterization of Hydroxyapatites: Identification of the Two Calcium Sites. *Magn. Reson. Chem.* **2008**, *46*, 347–350.
- (7) MacKenzie, K. J. D.; Smith, M. E. *M multinuclear Solid State NMR of Inorganic Materials*; Pergamon: Oxford, U.K., 2002.
- (8) Kolodziejski, W.; Klinowski, J. Kinetics of Cross-Polarization in Solid-State NMR: A Guide for Chemists. *Chem. Rev.* **2002**, *102*, 613–628.
- (9) Hayakawa, S.; Kanaya, T.; Tsuru, K.; Shiroasaki, Y.; Osaka, A.; Fujii, E.; Kawabata, K.; Gasqueres, G.; Bonhomme, C.; Babonneau, F.; et al. Heterogeneous Structure and In Vitro Degradation Behavior of Wet-Chemically Derived Nanocrystalline Silicon-Containing Hydroxyapatite Particles. *Acta Biomater.* **2013**, *9*, 4856–4867.
- (10) Kolmas, J.; Jaklewicz, A.; Zima, A.; Bućko, M.; Paszkiewicz, Z.; Lis, J.; Śłosarczyk, A.; Kolodziejski, W. Incorporation of Carbonate and Magnesium Ions into Synthetic Hydroxyapatite: The Effect on Physicochemical Properties. *J. Mol. Struct.* **2011**, *987*, 40–50.
- (11) Vyalikh, A.; Simon, P.; Rosseeva, E.; Buder, J.; Kniep, R.; Scheler, U. Intergrowth and Interfacial Structure of Biomimetic Fluorapatite–Gelatin Nanocomposite: A Solid-State NMR Study. *J. Phys. Chem. B* **2014**, *118*, 724–730.
- (12) *NMR Crystallography*; Harris, R. K.; Wasylshen, R. E.; Duer, M. J., Eds.; Wiley: Chichester, U.K., 2009.
- (13) Stejskal, E. O.; Memory, J. D. *High-Resolution NMR in the Solid State: Fundamentals of CP/MAS*; Oxford University Press: Oxford, U.K., 1994.
- (14) Hurle, K.; Neubauer, J.; Bohner, M.; Doeblin, N.; Goetz-Neunhoeffer, F. Effect of Amorphous Phases During the Hydraulic Conversion of Alpha-TCP into Calcium-Deficient Hydroxyapatite. *Acta Biomater.* **2014**, *10*, 3931–3941.
- (15) Akazawa, H.; Ueno, Y. Control of Composition and Crystallinity in Hydroxyapatite Films Deposited by Electron Cyclotron Resonance Plasma Sputtering. *J. Phys. Chem. Solids* **2014**, *75*, 94–99.
- (16) Garskaite, E.; Gross, K. A.; Yang, S. W.; Yang, T. C. K.; Yang, J. C.; Kareiva, A. Effect of Processing Conditions on the Crystallinity and Structure of Carbonated Hydroxyapatite (CHAp). *Cryst. Eng. Comm* **2014**, *16*, 3950–3959.

- (17) Uysal, A.; Stripe, B.; Lin, B. H.; Meron, M.; Dutta, P. Assembly of Amorphous Clusters under Floating Monolayers: A Comparison of In Situ and Ex Situ Techniques. *Langmuir* **2013**, *29*, 14361–14368.
- (18) Du, L. W.; Bian, S.; Gou, B. D.; Jiang, Y.; Huang, J.; Gao, Y. X.; Zhao, Y. D.; Wen, W.; Zhang, T. L.; Wang, K. Structure of Clusters and Formation of Amorphous Calcium Phosphate and Hydroxyapatite: From the Perspective of Coordination Chemistry. *Cryst. Growth Des.* **2013**, *13*, 3103–3109.
- (19) Landi, E.; Tampieri, A.; Cellotti, G.; Sprio, S. Densification Behavior and Mechanisms of Synthetic Hydroxyapatites. *J. Eur. Ceram. Soc.* **2000**, *20*, 2377–2387.
- (20) Rancourt, D. G.; Dang, M. Z. Absolute Quantification by Powder X-Ray Diffraction of Complex Mixtures of Crystalline and Amorphous Phases for Applications in the Earth Sciences. *Am. Mineral.* **2005**, *90*, 1571–1586.
- (21) Abrosimova, G. E.; Aronin, A. S.; Kholstina, N. N. On the Determination of the Volume Fraction of the Crystalline Phase in Amorphous-Crystalline Alloys. *Phys. Solid State* **2010**, *52*, 445–451.
- (22) Müller, L.; Kumar, A.; Baumann, T.; Ernst, R. R. Transient Oscillations in NMR Cross-Polarization Experiments in Solids. *Phys. Rev. Lett.* **1974**, *32*, 10402–1406.
- (23) Hester, R. K.; Ackermann, J. L.; Cross, V. R.; Waugh, J. S. Resolved Dipolar Coupling Spectra of Dilute Nuclear Spins in Solids. *Phys. Rev. Lett.* **1975**, *34*, 993–995.
- (24) Alemany, L. B.; Grant, D. M.; Alger, T. D.; Pugmire, R. J. Cross Polarization and Magic Angle Sample Spinning NMR Spectra of Model Organic Compounds. 3. Effect of the  $^{13}\text{C}$ - $^1\text{H}$  Dipolar Interaction on Cross Polarization and Carbon-Proton Dephasing. *J. Am. Chem. Soc.* **1983**, *105*, 6697–6704.
- (25) Ando, S.; Harris, R. K.; Reinsberg, S. A. Analysis of Cross-Polarization Dynamics between Two Abundant Nuclei,  $^{19}\text{F}$  and  $^1\text{H}$ , Based on Spin Thermodynamics Theory. *J. Magn. Reson.* **1999**, *141*, 91–103.
- (26) Thrippleton, M. J.; Cutajar, M.; Wimperis, S. Magic Angle Spinning (MAS) NMR Linewidths in the Presence of Solid-State Dynamics. *Chem. Phys. Lett.* **2008**, *452*, 233–238.
- (27) Bertani, P.; Raya, J.; Reinheimer, P.; Gougeon, R.; Delmotte, L.; Hirschinger, J.  $^{19}\text{F}$ / $^{29}\text{Si}$  Distance Determination in Fluoride-Containing Octadecasil by Hartmann-Hahn Cross-Polarization under Fast Magic-Angle Spinning. *Solid State NMR* **1999**, *13*, 219–229.